Pergamon

Int. J. Heat Mass Transfer. Vol. 41, No. 2, pp. 275–285, 1998

Printed in Great Britain
0017–9310/98 $19.00+0.00

PII: S0017–9310(97)00144–0

Inverse estimation of surface heat flux distributions during high speed rolling using remote thermal measurements

RUSSELL G. KEANINI

Department of Mechanical Engineering and Engineering Science, University of North Carolina at Charlotte, Charlotte, NC 28223-0001, U.S.A.

(*Received* 14 *November* 1996 *and in final form* 14 *May* 1997)

Abstract—An inverse method suitable for use with remote temperature measurements, is used to estimate time-dependent, axially-varying surface heat flux distributions during rolling. It is found that the diffusive time scale between the roll surface and the embedded measurement array determines the data sample rate and the solution's temporal resolution. The inverse method is first validated using simulated data from two representative measurement configurations. Following validation, the method is applied to experimental measurements from an instrumented work roll; flux distributions in this case are reconstructed over a period of approximately 3 h. Finally, a simple technique for regularizing temporally discontinuous flux distributions is introduced and demonstrated. © 1997 Elsevier Science Ltd.

INTRODUCTION

In high-speed rolling, a workpiece is plastically deformed during passage between two counter-rotating work rolls (see Fig. 1). A number of coupled, transient modes of heat transfer typically accompany this process, including conductive heat transfer across the roll-workpiece contact zone (roll bite), extreme, possibly temperature dependent frictional heating within the roll bite, forced convective cooling due to sprayed and jetted coolants and lubricants along the roll surface, and radiant exchange over portions of the roll surface at high workpiece temperatures.

Determining and controlling in-process roll temperatures constitutes a long-standing materials processing problem. Time dependent thermal strains within the roll, for example, can degrade workpiece surface quality [1], can introduce spatial nonuniformity within the workpiece [2], and can shorten roll service life [2, 3]. Similarly, suboptimal roll cooling can unnecessarily increase lubrication and/or cooling costs [4]. Importantly, development of robust thermal process control strategies or accurate thermal models rests on experimentally-based characterization of the time- and space-dependent surface heat flux (or temperature) distribution. Such information provides control or process models with *the* critical, theoretically insoluble boundary condition at the roll surface.

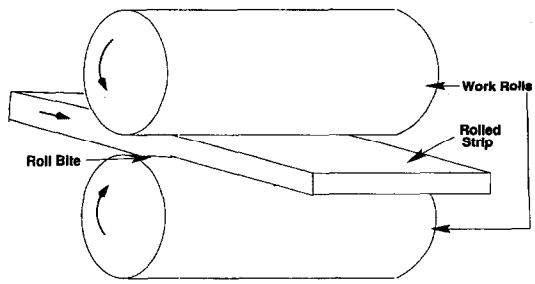

Fig. 1. Typical rolling process.

One of the two approaches can be taken in obtaining information on surface heating. In the first approach, surface heat fluxes or temperatures are measured directly [3–5]. This approach has proven difficult, however, due to extreme pressures and temperatures at the roll surface. The second approach, which bypasses direct surface measurements, is based on an indirect or inverse strategy and *estimates* surface conditions based on measurements within the roll.

Due to the lower experimental demands associated with indirect approaches, this area has attracted significant recent attention. Tseng *et al.* [1], for example, developed a one-dimensional finite element procedure to predict the time-varying circumferential surface heat flux distribution (at a single axial position) during water-cooled hot rolling (where the axial direction is determined by the roll's axis of rotation). In an extension of this approach, Huang *et al.* [6] accounted for azimuthal conduction in a two-dimensional inverse procedure, again predicting time-dependent circumferential heat flux distributions at a single axial location. Finally, some of these earlier finite element-based inverse results were reproduced by Johnson and Keanini [7] using an analytical approach.

The purpose of this paper is to develop an inverse method for estimating time-dependent, spatially varying surface heat flux distributions based on remote, subsurface temperature or heat flux measurements. (*Remote measurements* refer to measurements

NOMENCLATURE

$[C]$; C_{ij} global mass matrix; component in element mass matrix
c_p: $\hat{c}_p$ specific heat; dimensionless function describing temperature dependence of c_p
$[f]$; f_i global force vector; element force vector component
$f(r, z)$ initial temperature distribution
H function defined in equation (7a)
h dimensionless time step
k; $\hat{k}$ thermal conductivity; temperature dependence of k
$[K]$; K_{ij} global stiffness matrix; component in element stiffness matrix
L dimensionless length
N number of measurement sites
N_q number of parameters describing instantaneous flux distribution
$\mathbf{q}$ vector of parameters describing instantaneous surface flux distribution
q^*, q dimensional and dimensionless heat flux
R^*, R dimensional and dimensionless roll radius
r^*, z^*; r, z dimensional and dimensionless radial and axial coordinates
S_{n+1} augmented sum of squares function defined in equation (3)
t^*, t dimensional and dimensionless time
T dimensional temperature
U Heaviside unit step function
$X_{k,n}$ sensitivity coefficient
$Y_{j,n+1}$ measured temperature at location j, time t_{n+1}.

Greek symbols

α thermal diffusivity
β modified first order regularization term given by equation (3b)
γ_R regularization parameter
δ_P characteristic depth of embedded temperature probes
δ_T thermal boundary layer thickness
Δ^*; Δ dimensional and dimensionless time increment between successive workpieces
Δt dimensional time interval for averaging conduction equation
ΔT_s dimensional temperature scale
ε_i random error in ith temperature measurement
ε_q maximum acceptable change in local flux component (between times t_n and t_{n+1})
ε_T root mean square temperature error
ζ function defined in equation (3c)
η Gaussian random number
θ dimensionless temperature
ρ; $\hat{\rho}$ density; dimensionless function describing temperature dependence of ρ
σ dimensionless standard deviation
τ characteristic (dimensional) time scale
ϕ_i finite element weighting function
Ω roll rotation rate.

Subscripts

A advective
D diffusive
i inner; index for global force vector; weight function index
k index indicating axial position
n time index
R roll
α spatial differentiation index.

obtained outside the near-surface thermal boundary layer and are used to circumvent problems associated with sensor and roll surface degradation). While it is shown that remote measurements limit temporal resolution, reduce problem sensitivity, and constrain data sampling rates, it is nevertheless found that accurate inverse solution strategies can be developed.

A two-dimensional finite element-based procedure for estimating time dependent, *axially-varying* surface heat flux distributions is described. In order to allow temperature measurements external to near-surface thermal boundary layers, we base the formulation on a diffusive time-scale, $\tau_D = \delta_P^2 \alpha_o$, where α_o is the roll's characteristic thermal diffusivity and δ_p is the characteristic depth of probes embedded within the roll. On this scale, due to high roll rotation rates, angular variations in the surface flux distribution and roll temperature field can be neglected. This approach contrasts significantly with earlier investigations [1, 6] which, due to the availability of surface and near-surface measurements, focused on relatively short advective time-scale heat transfer ($\tau_A = \Omega^{-1}$). The inverse procedure is validated using simulated data, based on two representative measurement configurations. The first configuration, which replicates the remote sensor arrangement in an experimental work roll, allows us to determine proper data sampling rates and parameterization schemes for analyzing experimental data. The second (near-surface) configuration is used to examine the inverse code's

capabilities under highly dynamic surface heating conditions. Once validated, the method is used to determine flux distributions on the experimental work roll.

DIRECT HEAT TRANSFER MODEL

The experimental work roll is fitted with an array of 24-embedded thermocouples, as shown schematically in Fig. 2(a). From this figure it is seen that the thermocouples nearest the roll surface are located at a finite depth below the surface. Denoting this distance as δ_p, it is clear that a time interval $\tau_D = (\delta_p^2/\alpha_o)^{1/2}$ must elapse before thermal information diffuses from the surface to the outer-most measurement sites. Since surface flux variations over time scales shorter than τ_D are lost to diffusion, τ_D determines the inverse solution's approximate temporal resolution. Similarly, since estimation of azimuthal surface flux variations requires measurement resolution on the order of $\tau_A \equiv \Omega^{-1}$, where $\tau_D/\tau_A \gg 1$ in the present experimental system, it is clearly impossible to resolve circumferential flux distributions within this system. (Note that the inverse problems treated by Tseng *et al.* [1] and Huang *et al.* [6] were based on surface and near-surface temperature measurements and thus were not subject to diffusive time lag).

Considering the direct heat transfer problem, since the maximum temporal resolution is τ_D, then τ_D defines the relevant heat transfer time scale. In addition, since azimuthal flux variations are smeared by diffusion on this scale, azimuthal variations are neglected [7]. The equation governing the direct problem is obtained by performing a local energy balance over a time increment Δt which is short relative to τ_D, but long relative to τ_A. The requirement $\Delta t \ll \tau_D$ is imposed to allow temperature measurements over time intervals shorter than τ_D while $\Delta t \gg \tau_A$ allows smoothing of azimuthal property variations. (Note, under the conditions considered here, $\tau_D \sim 181$ s and $\tau_A \sim 1$ s). The resulting dimensionless equation has the familiar form

$$\hat{\rho}\hat{c}_p\theta_{,t} = \nabla \cdot (\hat{k}\nabla\theta) \tag{1}$$

where $\theta = (T - T_\infty)/(q_0/k)$, $\nabla = \hat{e}_r\partial/\partial r + \hat{e}_z\partial/\partial_z$, $r = r^*/\delta_p$, $z = z^*/\delta_p$, and $t = t^*/(\delta_p^2/\alpha_0)$, and where q_o is the characteristic workpiece-to-roll heat flux. Temperature dependent thermal properties are expressed as $k(\theta) = k_o\hat{k}(\theta)$, $\rho(\theta) = \rho_o\hat{\rho}(\theta)$, and $c_p(\theta) = c_{po}\hat{c}_p(\theta)$. As has been recently shown [7], equation (1) can also be derived using a multiple time scale asymptotic approach.

The boundary conditions are chosen to reflect conditions expected in the experimental work roll [refer to

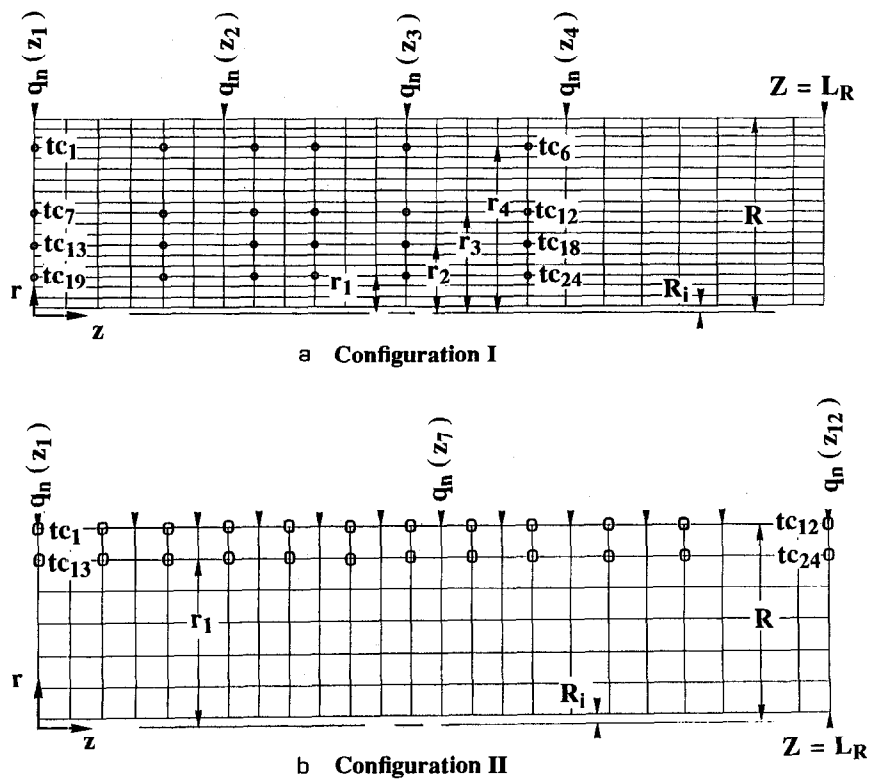

Fig. 2. Temperature measurement configurations: (a) experimental system and Case I configuration; (b) Case II configuration. The 24 measurement sites are numbered from left to right, top to bottom, as shown. The 12 flux parameters in Case II are likewise numbered left to right and are located at the inward pointing arrow-heads. The roll midline and end face are located at $z = 0$ and $z = L_R$, respectively. Dimensionless distances are listed in the text.

Fig. 2(a)]. It is assumed that heat transfer is symmetric about the roll midline. Thus, we confine calculations to half the roll and impose a symmetry condition at the midplane

$$\frac{\partial\theta}{\partial z}=0 \quad z=0. \tag{1a}$$

Consistent with experimentally observed temperature profiles, we also assume that axial temperature gradients disappear as the ends of the roll are approached. Thus,

$$\frac{\partial\theta}{\partial z}=0 \quad z=L_{\mathrm{R}} \tag{1b}$$

where L_{R} is the dimensionless roll half-width. A small hole is drilled down the roll's axis of rotation [see Fig. 2(a)]. Again, based on experimental temperature profiles, we assume that the radial temperature gradient is zero at all points along the hole surface:

$$\frac{\partial\theta}{\partial r}=0 \quad r=R_i \tag{1c}$$

where R_i the dimensionless hole radius. Along the role's outer surface, the boundary condition is expressed in terms of the unknown flux distribution q:

$$\hat{k}\frac{\partial\theta}{\partial r}=q(R,z,t) \tag{1d}$$

where $q=q^*/q_{\mathrm{o}}$. As described below, a time- and space-dependent parameterization is chosen to describe q, where the parameters are determined in sequential fashion by the inverse code. Finally, the initial condition is given by

$$\theta(r,z,t=0)=f(r,z) \tag{1e}$$

where $f(r,z)$ is zero in validation tests and is set equal to an experimentally determined nondimensional initial temperature in tests involving experimental temperature data.

INVERSE METHOD

Direct solution

The direct problem is solved using the Galerkin finite element method and implicit time stepping. The resulting system of equations is given by:

$$([C]+h\gamma[K])\theta_{n+1} = ([C]-h(1-\gamma)[K])\theta_n+h\gamma\mathbf{f}_{n+1}+h(1-\gamma)\mathbf{f}_n \tag{2}$$

where subscripts denote the time index and where elements of the mass and stiffness matrices are given by

$$C_{ij}=\int_{V_{\mathrm{e}}}\hat{\rho}\hat{c}_{\mathrm{p}}\phi_i\phi_j\,\mathrm{d}V \tag{2a}$$

$$K_{ij}=\int_{V_{\mathrm{e}}}\hat{k}\phi_{i,\alpha}\phi_{j,\alpha}\,\mathrm{d}V. \tag{2b}$$

Here, h is the dimensionless time step, γ is a constant between 0 and 1 ($\gamma=1/2$ here), and V_{e} is the element volume. Suppressing the time index, force vector elements are given by

$$f_i=\int_{S_{\mathrm{e}}}\phi_i q\,\mathrm{d}S \tag{2c}$$

where $q=\hat{k}\partial\theta/\partial n$ is again the dimensionless, time dependent heat flux and S_{e} is the element surface. Under the experimental conditions considered here, roll temperatures vary by a maximum of approximately 44°C. In cases where temperature, and thus property variations are significant, iterative under-refluxation is performed at each time step.

Regularization

In some of the examples discussed below, inverse solutions are stabilized using first order regularization in time [8, 9]. At each time step during the inverse procedure, the following augmented sum of squares function is thus minimized:

$$S_{n+1}=\sum_{j=1}^{N}(Y_{j,n+1}-\theta_{j,n+1})^2+\gamma_{\mathrm{R}}\beta(q_{n+1}) \tag{3}$$

where

$$\beta=\sum_{j=1}^{N_q}[q_{j,n+1}-q_{j,n}]^2 \tag{3a}$$

and where N is the number of measurement sites, γ_{R} is the regularization parameter, N_q is the number of parameters describing the instantaneous surface flux distribution, n is the time index, and U is the Heaviside function.

As described below, we will use a modified form of equation (3a) in one of the runs performed in Case II:

$$\beta=\sum_{j=1}^{N_q}[q_{j,n+1}-q_{j,n}]^2[1-U(\zeta_{j,n+1}-\varepsilon_q)] \tag{3b}$$

where $\zeta_{j,n+1}$ is given by

$$\zeta_{j,n+1}=\max\left[\frac{|q_{j,n+1}|}{|q_{j,n}|},\frac{|q_{j,n}|}{|q_{j,n+1}|}\right]. \tag{3c}$$

As discussed below, this modification is designed to eliminate artificial smoothing of temporally discontinuous flux components, typical in rolling. Notice that the size of the discontinuities preserved is determined by the magnitude of ε_q (where $\varepsilon_q=0.1$ in the case mentioned).

The regularization parameter γ_{R} is determined by finding the value that yields [9, 10]

$$\sum_{i=1}^{N}\left[\frac{(Y_i-T_i)}{\sigma_i}\right]^2\approx N-N_q \tag{4}$$

where T_i is the instantaneous calculated temperature at measurement location i and σ_i is the corresponding

standard deviation. In all cases, we assume σ_i equals a constant σ, where

$$\sigma \Delta T_s = \sigma^* \approx \sqrt{\overline{\varepsilon_T^2}}. \quad (5)$$

Here, σ^* is the dimensional standard deviation, $\Delta T_s = q_o/k_o$ is the dimensional temperature scale, and $\sqrt{\overline{\varepsilon_T^2}}$ is the characteristic rms measurement error. The last approximation incorporates the standard assumptions that measurement errors are additive, have zero mean, are fixed in time and are normally distributed [10].

Algorithm

At any given time, t_n, the inverse algorithm determines N_q nodal surface fluxes, $q_{k,n} = q(z_k, t_n)$, where the z_ks define $z_k - 1$ approximately equal intervals along the roll axis and where linear flux variations are assumed between adjacent z_ks. Letting $\mathbf{q}_n$ be the vector of nodal fluxes determined at t_n, the following procedure is used to determine $\mathbf{q}_{n+1}$:

(i) Starting from an initial guess for $\mathbf{q}_{n+1}$, iteratively solve the direct problem in equation (2) to minimize the augmented least-square error $S_{n+1} = S(\mathbf{q}_{n+1})$ defined in equation (3).

(ii) Once S_{n+1} is minimized, take the corresponding minimizing $\mathbf{q}$ as $\mathbf{q}_{n+1}$ and return to step (i).

Minimization is performed using the conjugate gradient technique [11]; due to sometimes rapid variations in local surface heat fluxes, $\mathbf{q}_{n+1}$ is set equal to zero at the start of each minimization. Figure 3 summarizes the direct model and inverse approach.

SENSITIVITY CHARACTERISTICS

As discussed below, stable and accurate non-regularized inverse solutions cannot be obtained when temperature measurement sites lie far outside the near-surface thermal boundary layer. Insight into the difficulties associated with remote temperature sensing can be gained by considering the problem defining the sensitivity $X_{k,n} = \partial\theta/\partial q_{k,n}$, where $q_{k,n} = q(R, z_k, t_n)$. Based on assumed linearity, $X_{k,n}$ satisfies the equation governing θ [equation (1)], a zero initial condition, and the boundary conditions, (1a)–(1c). In addition, due to assumed linear variations between adjacent flux components comprising $\mathbf{q}_n$, the boundary condition (1d) assumes the form $\hat{k}\, X_{k,n,r} = g(z, t)$ where $g(z, t)$ is zero, except over the interval $t_n \leqslant t \leqslant t_{n+1}$. Over this interval, $g(z, t)$ describes a triangularly shaped function that increases linearly from 0 to 1 over (z_{k-1}, z_k), and then decreases linearly back to 0 over (z_k, z_{k+1}). Thus, by consideration of the problem governing $X_{k,n}$, we can make several observations: (i) over $t_n \leqslant t \leqslant t_{n+1}$, sensitivity to the kth instantaneous flux parameter diffuses outward (on a diffusive time scale τ_D) from a source centered at z_k; (ii) while the source at z_k is active (over $t_n \leqslant t \leqslant t_{n+1}$), a global sensitivity maximum exists at $(r, z) = (R, z_k)$; this follows since lines of constant sensitivity are normal to all boundaries (except in the neighborhood of z_k) and since sensitivity should not increase as roll corners are approached; (iii) once the source at z_k becomes inactive (over $t > t_n$), a bubble-shaped high sensitivity

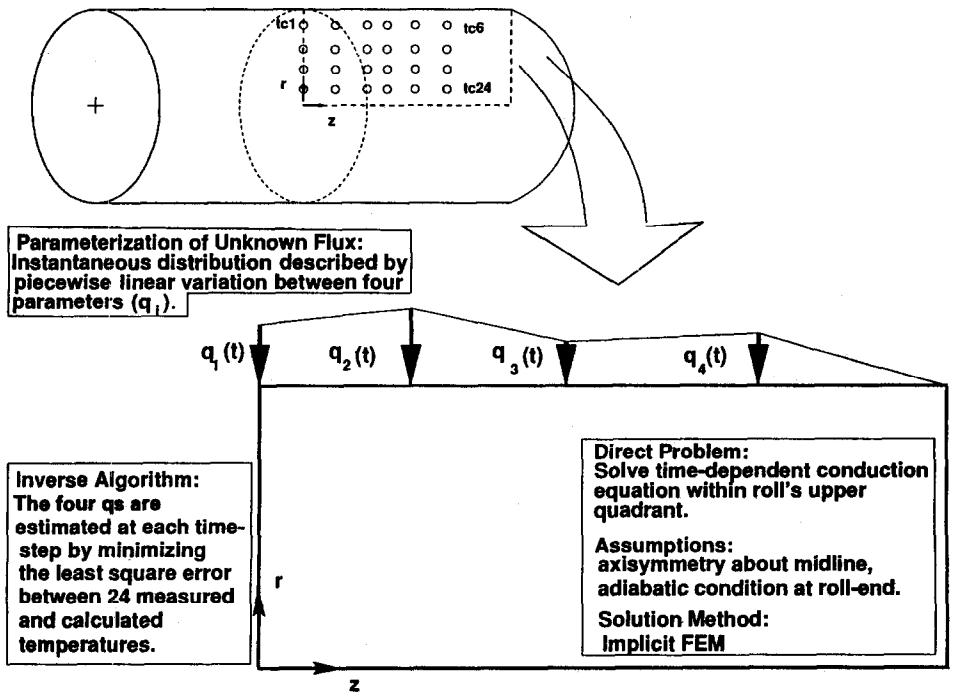

INVERSE METHOD AND DIRECT MODEL

Fig. 3. Schematic description of the direct model and inverse method.

region forms and diffuses toward the roll's axis of rotation; (iv) initially, this region's lateral extent is on the order of $z_{k+1}-z_{k-1}$ $(=l_k)$ while its radial extent is on the order of $(t_{n+1}-t_n)^{1/2}$; both dimensions increase like $(t-t_{n+1})^{1/2}$, however, as the bubble moves across the roll.

Since the dimensional time required for the high sensitivity bubble to reach most of the probe array is on the order of R^{*2}/α_o, the bubble's lateral extent increases to a dimensional length of $l_k^*+(\alpha_o R^{*2}/\alpha_o)^{1/2}=l_k^*+R^*(=l_k\,\delta_D)$. In the present experimental system, the characteristic lateral dimension of the high sensitivity region, l_k, is on the order of $3R^*/\delta_p$, while the characteristic lateral spacing Δz_m between measurement sites is on the order of $R^*/(2\delta_p)$. Thus, since the corresponding lateral gradient in $X_{k,n}$ is on the order of $X_{k,n}/l_k$, the Taylor expansion relating sensitivities at laterally adjacent measurement sites, $X_{k+1,n}=X_{k,n}+X_{k,n,z}\Delta z_m$, reveals that lateral sensitivity changes are small. (A similar argument applies in the radial direction). Thus, any change in a given flux parameter produces an essentially space-invariant temperature response across the measurement region (see Case I below) and largely explains why inverse solutions are difficult to obtain with a remote sensing arrangement.

CODE VALIDATION AND TESTING

Since inverse solutions are given to instability, it is important to ensure that an experimental system has sufficient sensitivity to allow accurate inverse solutions. In addition, since a remote measurement configuration is used in the experiment described below, we find we must also examine the inverse method's temporal resolution. Thus, prior to applying the inverse procedure to experimental results, we perform tests using simulated data on a measurement configuration identical to that in the experimental work roll. This will be referred to as Case I. In order to test the inverse code's capabilities under highly dynamic surface heating conditions, we will also examine a test case where simulated measurements are obtained on and near the roll surface (Case II). The measurement configurations used in Cases I and II are shown in Figs. 2a and b, respectively. Note that Configuration II (Case II) is chosen to provide maximum sensitivity, maximum temporal resolution, and enhanced axial resolution.

Although the inverse code accommodates thermal property variations, incorporating full nonlinear direct solutions within an inverse calculation proves expensive, and for purposes of illustration and testing, is unnecessary. Thus, in both test cases, we fix property values at ρ_o, k_o and c_{po}. While the same simplification is used in analyzing experimental data below, the simplification is justified in this case since the characteristic temperature scale is only $\sim 44°$.

In both validation tests, measurement error is simulated by adding a random error component ε_i to the calculated temperatures:

$$Y_i = T_i+\varepsilon_i = T_i+\sigma\eta$$

where σ is the dimensionless standard deviation and η is a gaussian random number. Solution accuracy is determined at three level of error, $\sigma=10^{-6}$, $\sigma=0.0012$, and $\sigma=0.006$, where the first σ value simulates 'exact' temperature data [9]. Based on equation (5) (which shows that $\sigma\approx\sqrt{\bar{\varepsilon}_T^2}/\Delta T_s$), and based on an assumed characteristic temperature scale of $\Delta T_s=460°C$ (in Cases I and II; see below), it is seen that the second and third σs correspond to rms measurement errors of 0.55°C (1F) and 2.77°C (5F), respectively.

In case I, it is found that accurate inverse solutions require relatively fine radial resolution; thus, an 18×24 finite element mesh is employed. Case II, in contrast, accommodates relatively course radial resolution and incorporates a 6×24 element mesh. [Note that while the fine mesh reduces radial discretization error by approximately 66% (linear elements), the direct solution cost (approximately proportional to the number of nodes cubed) increases by roughly 20-fold. For a given N_q, this translates into a 20-fold increase in inverse solution cost.] Interestingly, the improvement in direct solution accuracy is small; under Case I surface heating conditions, for example, nodal temperatures determined on the two meshes differ by less than 5% over the time span $0\leqslant t<\sim 45$. [While predicted fluxes for $t>\sim 45$ are, in both cases, within 1% of the actual flux, relative differences on the two meshes are significant. This apparently reflects round-off error, which in these calculations could be as high as $N_qN_n^3\varepsilon_m$, where $N_n(=475$ in Case I; $=175$ in Case II) is the number of nodes and ε_m $(\sim 10^{-8})$ is the machine accuracy [11].] Direct solution accuracy was validated using the analytical solution to a unit step-up in the boundary heat flux.

Except as noted, parameter values used in Cases I and II and in subsequent analysis of experimental data are as follows: $N=24$; $N_q=4$ (Case I and experiment), $N_q=12$ (Case II); $\gamma=1/2$; $\Delta T_s=460°C$ (Cases I and II), $\Delta T_s=44°C$ (experiment); $\delta_p=0.047$ m (Case I and experiment), $\delta_p=1.56\,(10^{-2})$ m (Case II); $\tau_D=181$ s (Case I and experiment), $\tau_D=20$ s (Case II); $T_\infty=22.2°C$; $k_o=42.3$ W m^{-1} K^{-1} [12]; $c_{po}=442.0$ J kg^{-1} K^{-1} [12]; $\rho_o=7858.0$ kg m^{-3} [12]; $\alpha_o=1.22\,(10^{-5})$ m^2 s^{-1}. (Note that material property values are those of steel. The values of τ_D and δ_p used in Case II are derived in the next section. In Cases I and II, inverse solutions are determined over the interval $0\leqslant t\leqslant 50$, while the experimental analysis is extended over the duration of the experiment, $0\leqslant t\leqslant 75$ (corresponding to a dimensional time of 2.92 h; see below). The dimensionless lengths shown in Fig. 2(a) are as follows: $r_1=1.35$, $r_2=2.43$, $r_3=3.51$, $r_4=5.67$, $R_i=0.270$, $R=6.67$, and $L_R=28.1$. Similarly, the lengths in Fig. 2(b) are: $r_1=17.1$, $R_i=0.814$, $R=20.1$, and $L_R=84.7$.

Time steps and reduced data sets in Case I and scaling issues in Case II

In the experimental analysis described below, the dimensionless time step h corresponding to the experimental simple rate Δt_e^* leads to unstable inverse solutions (in spite of regularization). (Note, the sample interval Δt_e^* is the time required to sample the array of 24 embedded thermocouples). Results presented by Beck *et al.* (see pp. 28–29 in [9]) and our discussion of sensitivity characteristics above, however, suggest that sensitivity can be maximized and stability possibly regained by choosing a sampling interval Δt_{er}^* that is approximately equal to the diffusion time scale τ_D. Thus, since $\tau_D = 181$ s and $\Delta t_e^* = 20$ s, a reduced data set $\mathbf{D}_r$ can be formed by sampling every ninth reading from the original data set **D**. Subsequent tests show that temporal resolution can be further reduced by sampling every seventh reading in **D**. Note, early tests implementing Beck's [9] sequential estimation method and based on the non-reduced data set **D** proved unsuccessful.) Thus, following formation of $\mathbf{D}_r$, the dimensionless time step used in analyzing experimental data is $h = \Delta t_{er}^*/\tau_D = 140/181 = 0.77$. Similarly, $h = 0.77$ in Case I.

In Case II, since the most sensitive probes are located on the probe surface, we are free to define a new length scale δ_p. In particular, the chosen scale should lead to stable inverse solutions while improving on Case I temporal resolution. A competing concern is that the sample interval Δt_e^* (which along with δ_p determines h) should be much longer than the roll rotation rate Ω (in order to ensure azimuthal smearing of properties). Thus, for a characteristic Ω of 1 s^{-1}, we arbitrarily set Δt_e^* equal to the same value used in the experiment (20 s) and take advantage of the indeterminate length scale to arbitrarily set h equal to 1. (Thus, δP, which equals $\sqrt{\Delta_e^* \alpha_o / h}$, has the value 1.56 ($10^{-2}$) m, while $\tau_D = \delta_P^2/\alpha_o = \Delta T_e^* = 20$ s.)

Case I validation—inverse solutions based on remote measurements

The flux distribution used to generate simulated data in this case [shown in Fig. 4(a)] is given by

$$q(R, z, t) = G_I(z) \cdot \exp(-\beta t) \tag{6}$$

where $G_I(z)$ is a piecewise continuous function representing a range of observed distributions (including the estimated experimental distribution) and β (= 0.1) is a constant. The exponential term is chosen to roughly simulate the flux decay observed during the hot soaking experiment described below. (Note, to better exercise the code, the decay rate in this case is made somewhat larger than the estimated experimental decay rate.)

The results, presented in part in Fig. 4, show that relatively accurate inverse solutions can be obtained at all levels of measurement error. Indeed, predicted distributions corresponding to exact measurements ($\sigma = 10^{-6}$) are essentially identical to the actual distribution (result not shown). As expected, solution instability amplifies as measurement error increases [where the result corresponding to $\sigma = 0.006$ is shown in Fig. 4(b)]. Although the regularization parameter γ_R is set equal to 0.07 at all three levels of error, similar results, satisfying equation (4), are obtained for $\gamma_R = 0.5$ and 0.05.

Based on a number of tests using a variety of flux distributions, it appears that inaccurate inverse solutions can be readily diagnosed in this configuration: large relative errors between simulated experimental temperatures and those determined by the inverse procedure are observed at the outermost (i.e. most sensitive) probe sites. This is a significant (though preliminary) finding which bears on the experimental analysis to follow.

Case II validation—inverse solutions based on surface measurements

As mentioned, this case is designed to examine the algorithm's capabilities under highly transient heating conditions; in contrast to Case I, the results have little diagnostic value in the experimental analysis. In this case, we simulate successive rolling of several workpieces, where each workpiece is separated by a fixed interval Δ. The flux distribution used to generate temperature data is shown in Fig. 5(a) and is given by

$$q(R, z, t) = G_{II}(z) \cdot H(t) \tag{7}$$

where

$$H(t) = \sum_{n=1}^{5} [U[t-(n-1)P] - U[t-(nP-\Delta)]] \tag{7a}$$

and where $G_{II}(z)$ is another representative continuous function. Here, $P-\Delta$ is the dimensionless time required to roll each workpiece. As mentioned, measurement Configuration II is employed in this case [Fig. 2(b)] and N_q is increased from 4 to 12.

As in Case I, the predicted flux distribution based on exact temperature data is found to be virtually indistinguishable from the actual distribution (result not shown). Relatively accurate inverse solutions also follow when measurement errors are moderate ($\sigma = 0.0012$), while accuracy and stability degrade at large measurement error ($\sigma = 0.006$). Refer to Figs. 5(b) and 6(a), respectively. Note that regularization is not used in obtaining the results shown in Figs. 5(b) and 6(a).

The result corresponding to $\sigma = 0.006$ [Fig. 6(a)] brings us to an important finding. If we attempt to control the instability depicted in Fig. 6(a) through standard first order regularization, the predicted flux distribution exhibits globally amplified instability and artificial smoothing during the low flux periods between rolling (result not shown). However, if we employ first-order regularization augmented with a ratio test, as embodied in equations (3b) and (3c), these pathological features are eliminated, and we obtain the result shown in Fig. 6(b). Thus, the poten-

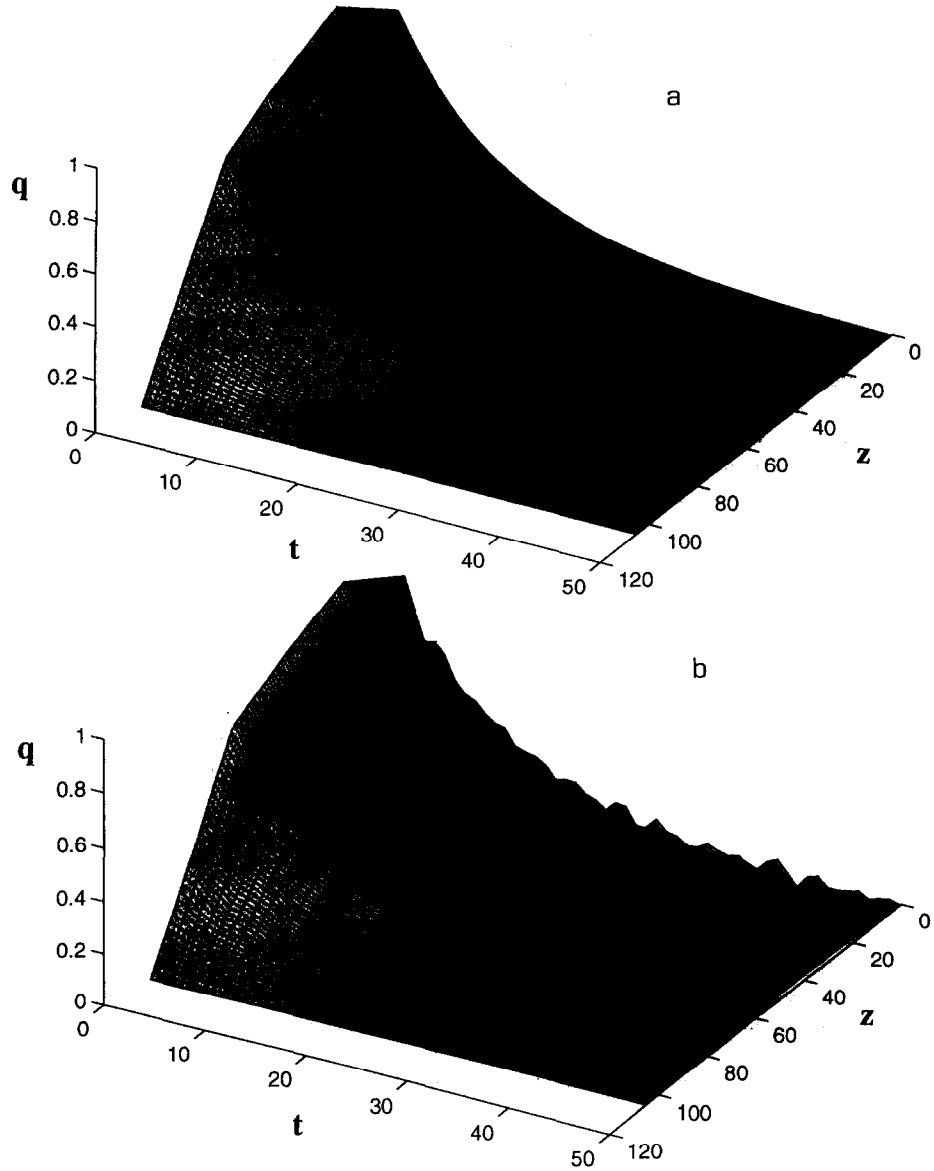

Fig. 4. Case I heat flux distributions: (a) actual distribution; (b) estimated distribution, $\sigma = 0.006$. Note, the graphical length scale is altered from the solution length scale (1 unit = 0.0127 m). Each time increment equals 140 s.

tial utility of incorporating a ratio test under highly transient heating conditions becomes apparent.

INVERSE ANALYSIS OF EXPERIMENTAL MEASUREMENTS

In this section, we analyze a set of measurements obtained during hot soaking prior to rolling. Here, a set of jets are turned on at time zero and left on for a period of approximately 3 h. The instrumented work roll rotates at a fixed rate throughout ($\Omega \sim 1\ s^{-1}$) and temperatures are sampled at a rate of 1.2 Hz. We will assume that the flux decays linearly to zero between z_4 and the end of the roll (at $z = L_R$); due to low sensitivity to imposed fluxes over $\sim z_4 < z < L_R$, it is found that predicted solutions are essentially independent of the assumed variation between z_4 and L_R.

Since 20 s ($= \Delta t_c^*$) elapse during every scan through the thermocouple array, measured temperatures in the original data set **D** are linearly interpolated to the start of each scan. Following this step, the reduced data set $\mathbf{D}_r$ is formed by sampling every mth member of **D** (where $m = 7$). Due to the time lag between initiation of the hot soaking operation and the start of detectable heating at the outermost probe sites, temperature readings remain essentially constant during the first 2.33 min. of the experiment. Thus, this data is not used in the inverse procedure. Attempting to include this data produces unstable inverse estimates, reflecting the fact that one cannot estimate surface heating

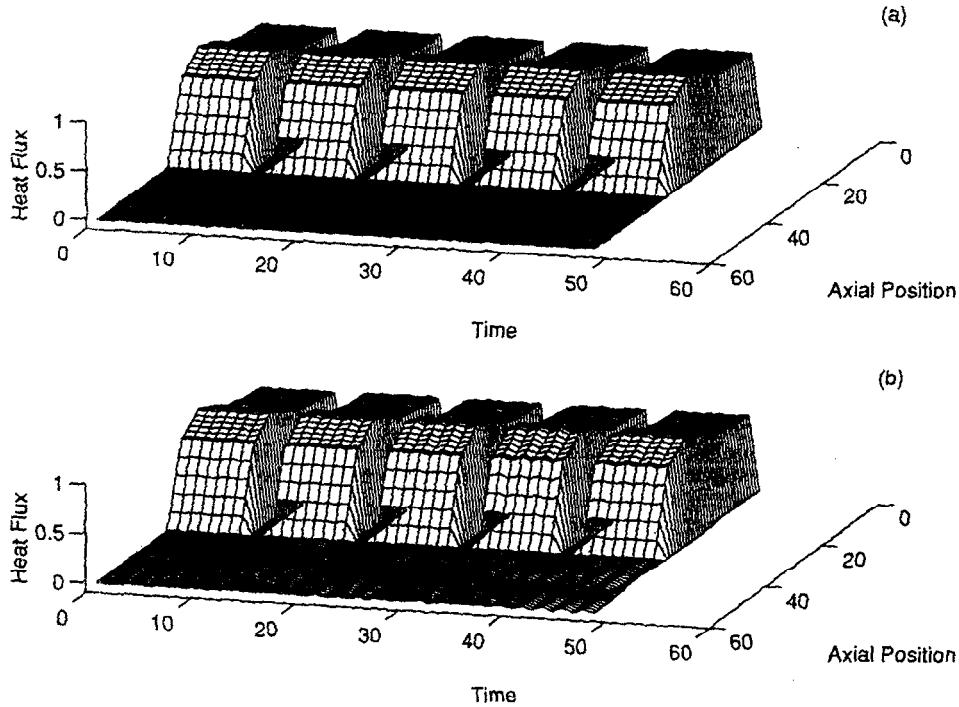

Fig. 5. Case II heat flux distributions: (a) actual distribution; (b) estimated (non-regularized) distribution, $\sigma = 0.0012$. The graphical length scale is altered from the solution length scale (1 unit = 0.022 m). Each time increment equals 20 s.

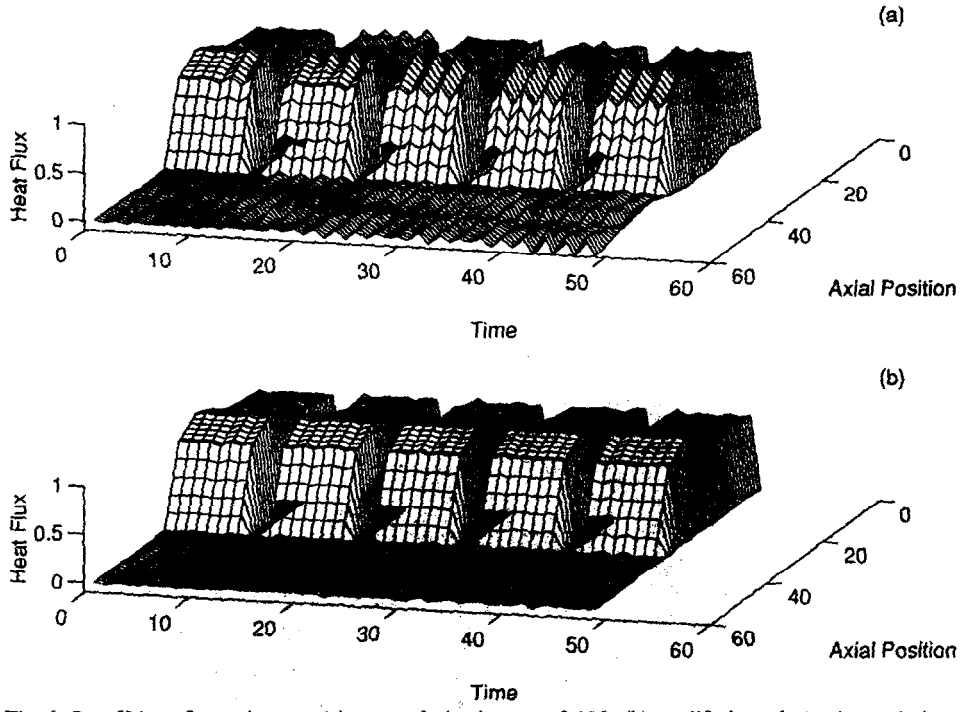

Fig. 6. Case II heat flux estimates: (a) no regularization, $\sigma = 0.006$; (b) modified regularization technique given by equations (3b) and (3c); $\sigma = 0.006$. The graphical length scale is altered from the solution length scale (1 unit = 0.022 m). Each time increment equals 20 s.

conditions *before* thermal information can be detected.

Predicted and measured temperatures at measurement sites nearest the roll surface and nearest the roll axis are shown in Figs. 7 and 8, respectively. Clearly, excellent agreement is observed nearest the roll surface, while fair agreement is observed near the roll axis. Although not shown, the level of agreement

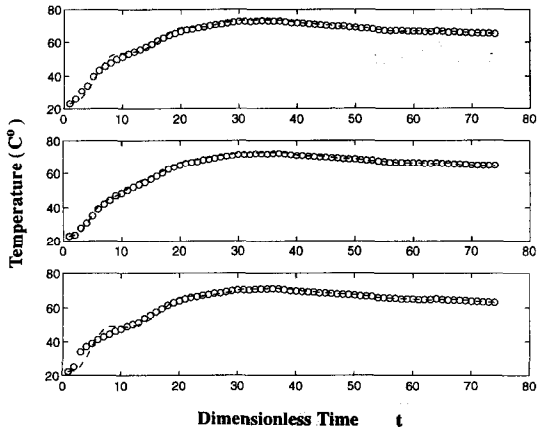

Fig. 7. Comparison between predicted (——) and experimentally measured (o) temperatures at outermost probe sites. The upper graph corresponds to measurement site 1, the middle graph to site 3, and the lower graph to site 6 [refer to Fig. 2(a)]. Each time increment equals 140 s.

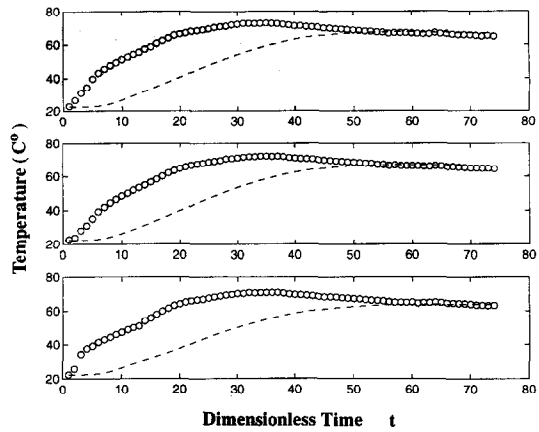

Fig. 8. Comparison between predicted (——) and experimentally measured (o) temperatures at innermost probe sites. The upper graph corresponds to measurement site 19, the middle graph to site 21, and the lower graph to site 24 [refer to Fig. 2(a)]. Each time increment equals 140 s.

improves as one proceeds from the innermost to the outermost row of thermocouples. In addition, axial variations in calculated temperatures decrease with decreasing radius, resulting in increasingly uneven levels of agreement along any given radius (Fig. 8). In terms of sensitivity characteristics, the first trend reflects diffusive decay of peak sensitivity (as we progress across the roll radius), while the second trend reflects associated diffusive smearing of sensitivity gradients.

The predicted flux distribution is shown in Fig. 9. The relatively large initial oscillation likely reflects solution instability rather than a real flux variation. This appears to be the case since oscillations are not observed in the experimental temperature measurements and since the oscillations can be smoothed (somewhat) by using a larger regularization parameter (not shown). Once the initial transient dies out, the predicted flux distribution undergoes a slow, essentially space invariant decay to zero (near ~ 70). Note that the predicted distribution is fully consistent with the nominally uniform spray pattern used during

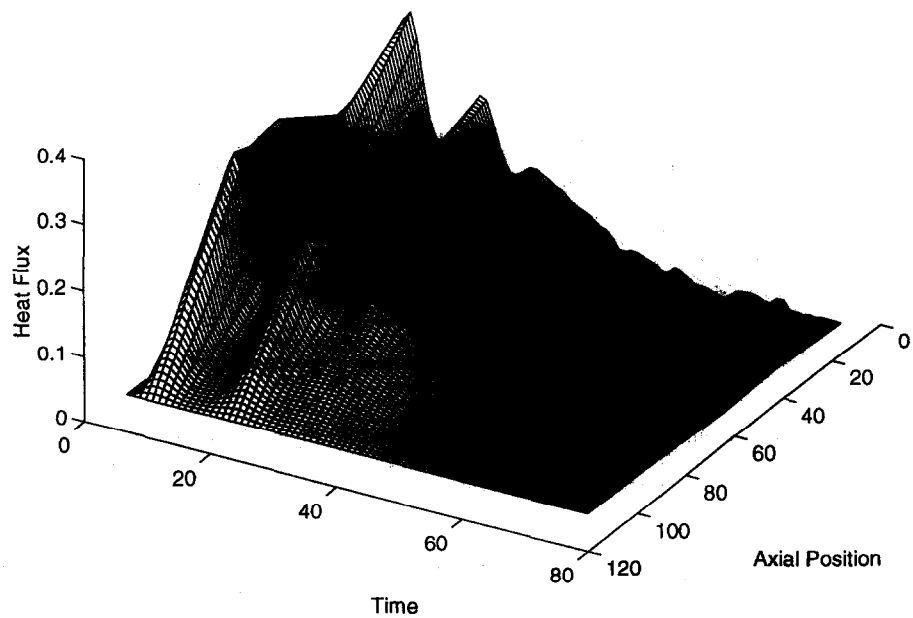

Fig. 9. Estimated experimental flux distribution. The graphical length scale is altered from the solution length scale (1 unit = 0.0127 m). Each time increment equals 140 s.

the hot soak. In addition, based on tests described in Case I, the close agreement between calculated and measured temperatures at the outermost probe sites provides indirect evidence that the estimated distribution is relatively accurate.

CONCLUSIONS

An inverse algorithm for estimating diffusive time scale surface heat flux distributions during rolling has been developed. The principal results and findings are as follows:

(1) Accurate inverse solutions under transient heating conditions can be obtained using both surface and remote temperature measurements.

(2) In order to prevent instability, a suitable data sample rate must be used. The rate is essentially determined by the diffusive transport time between the roll surface and the outermost probe sites.

(3) A modified regularization technique is introduced which allows accurate prediction of highly transient flux distributions (based on surface and near-surface temperature measurements).

(4) Analysis of experimental data obtained during hot soaking demonstrates that the inverse procedure is capable of accurately predicting measured temperatures over significant periods of time (the longest tests to date span 2.92 h).

(5) In the hot soaking experiment, the inverse code predicts a slowly decaying, essentially space invariant flux distribution. The estimated distribution is qualitatively consistent with the imposed heating pattern.

Acknowledgements--This work was supported by an Alcoa Foundation Science Support Grant, Gary Pallone and Mike Karabin project sponsors. Comments provided by Professors Robert Johnson and Harish Cherukuri are appreciated.

REFERENCES

1. Tseng, A. A., Chang, J. G., Raudensky, M. and Horsky, J., An inverse finite element evaluation of roll cooling in hot rolling of steels. *Journal of Material Processing and Manufacture Science*, 1995, **3,** 387–408.
2. Roberts, W. L., *Cold Rolling of Steel.* Marcel Dekker, New York, 1978, Chapter 3.
3. Tseng, A. A., Lin, F. H., Gunderia, A. S. and Ni, D. S., Roll cooling and its relationship to roll life. *Metallurgy Transactions*, 1989, **20A,** 2305–2320.
4. Jeswiet, J., Measuring metal deformation interface forces and temperatures. *CSME Transactions*, 1993, **17,** 633–645.
5. Hatamura, Y. and Yoneyama, T., Measurement of actual stress and temperature on the roll surface during rolling. *JSME International Journal Series III*, 1989, **32,** 676–685.
6. Huang, C. H., Ju, T. M. and Tseng, A. A., The estimation of surface thermal behavior of the working roll in hot rolling process. *International Journal of Heat and Mass Transfer*, 1995, **38,** 1019–1031.
7. Johnson, R. E. and Keanini, R. G., An asymptotic model of work roll heat transfer. *International Journal of Heat and Mass Transfer*, 1997 (submitted).
8. Tikhonov, A. N. and Arsenin, V. Y., *Solutions of Ill-Posed Problems.* Winston, Washington, D.C., 1977, Chapter 2.
9. Beck, J. V., Blackwell, B. and St Clair, C. R., *Inverse Heat Conduction.* Wiley, New York, 1985, p. 28.
10. Beck, J. V. and Arnold, K. J., *Parameter Estimation in Engineering and Science.* Wiley, New York, 1977, Chapter 1.
11. Press, W. H., Teukolsky, S. A., Vetterling, W. T. and Flannery, B. P., *Numerical Recipes*, 2nd edn. Cambridge University Press, New York, 1992, p. 19.
12. Incropera, F. P. and DeWitt, D. P., *Fundamentals of Heat and Mass Transfer*, 4th edn. Wiley, New York, 1996, Appendix A.